https://doi.org/10.1016/j.partic.2018.02.003 **This is the Pre-Published Version.**

Numerical simulation of particle formation and evolution in a vehicle exhaust plume using the bimodal Taylor expansion method of moments

Shuyuan Liu, Tat Leung Chan*, Huijie Liu

Department of Mechanical Engineering, The Hong Kong Polytechnic University, Kowloon, Hong Kong, China
*Corresponding Author. E-mail: mmtlchan@polyu.edu.hk (T.L. Chan)

Abstract The bimodal Taylor expansion method of moments (B-TEMOM) model scheme was developed to simulate the formation and evolution of vehicle exhaust particles. Two independent types of log-normal particle size distributions were selected in the B-TEMOM model scheme, comprising large and small particles to represent background (i.e., the surrounding environment) and vehicle exhaust particles, respectively. Concentration distributions of exhaust and background particles derived using this model scheme were validated against results from a moving sectional method and the bimodal quadrature method of moments, showing excellent agreement. The effects of vehicle tailpipe exit conditions (e.g., exhaust particle concentrations and velocity), sulfur content, and relative humidity on the evolution of particles were investigated numerically. Both two-dimensional and three-dimensional numerical simulations showed that tailpipe exit velocity and relative humidity did not greatly affect the steady-state concentrations or the diameters of particles in urban atmospheres. Although an increase in sulfur content had little effect on the particle concentration, it led to background particles with larger geometric average diameter entering the environment. This coupled CFD-B-TEMOM numerical model provides a simple but accurate and efficient method for studying bimodal aerosol dynamics.

Keywords: Vehicle exhaust particles; Bimodal Taylor expansion method of moments; Homogeneous nucleation; Coagulation; Tail pipe exit velocity; Sulfur content and ambient relative humidity

1. Introduction

Particulate matter (PM) emission has become a concern because of its harmful effect on human health (Pope et al., 2004; Araujo & Nel, 2009; Tie & Cao, 2009; González & Rodríguez, 2013; Kim, Kabir, & Kabir, 2015; Li, Wen, & Zhang, 2017), as well as its effects on the Earth's radiative balance and climate (Medina, Fitzgerald, & Min, 2012; Tang & Li, 2014; Ning et al., 2013) and on black soiling of buildings (Kittelson, 1998). Vehicle exhaust PM makes a major contribution to the ultrafine particles in urban atmospheres (Olin, Rönkkö, & Dal Maso, 2015). Many studies of the properties of vehicle exhaust PM have been published, including investigations of particle structure and particle size distributions (Yu, Lin, & Chan, 2008; Yu & Lin, 2009a, 2009b; Chan, Liu, & Chan, 2010; Yu, Lin, Jin, & Jiang, 2011; Alam et al. 2016; Sun, Zhou, & Wang, 2016), chemical properties (Chan & Ning, 2005; Chan, Zhou, & Lin, 2005; Wang, Chan, Cheung, Leung, & Hung, 2006; Alam et al., 2016), and compositions of various types of vehicle

exhausts (Rönkkö et al., 2007; Pant & Harrison, 2013; Alam et al., 2016). Vehicle exhaust PM is generally classified into two types, comprising solid and liquid particles (Morawska & Zhang, 2002). Unlike the solid particles generated during fuel combustion, liquid particles mainly form from cooling exhaust gases . These liquid particles are formed by nucleation of exhaust gases released from the vehicle tailpipe (Olin et al., 2015; Kittelson et al., 2008). As the particles formed by nucleation are very small (< 100 nm), a particle size distribution (PSD) is often measured to obtain general information about vehicle exhaust PM. In addition to the PSD, particle number and volume concentrations are also measured. Peng et al. (2014) measured these two parameters at 13 locations within China from October 2007 to November 2011. Kim et al. (2007) investigated the physical characteristics of particles (0.3−25 μm) at the Gosan super-site in South Korea in April 2001. Asmi et al., (2011) analyzed aerosol number size distributions from 24 European field monitoring sites from 2008 to 2009. Aerosol size distributions have also been measured in many megacities, such as New Delhi (Mönkkönen et al., 2005), Beijing (Wu et al., 2008; Yue et al., 2010), Guangzhou (Rose et al., 2010) and Paris (Freutel et al., 2013).

Numerical studies of aerosol particle properties also have been carried out using numerical simulation methods to overcome the complexity of aerosol dynamic processes (e.g., formation, evolution, and transport) within the atmosphere. Yu and Luo (2009) simulated particle size distributions using a global aerosol model to investigate the influence of nucleation on aerosol properties. Numerical methods, such as sectional methods (Liu, Yu, Yin, Jiang, & Chen, 2014), moment methods (McGraw, 1997; Yu & Lin, 2010; Yu, Zhang, Jin, Lin, & Seipenbusch, 2015; Yu & Chan, 2015; Chan, Liu, & Yue, 2018), and Monte Carlo methods (Chan et al., 2001; Liu & Chan, 2017; Liu H.M. & Chan, 2018), have been used to solve general dynamic equations for aerosol particles to obtain their evolution history within the atmosphere. Typical aerosol dynamic processes, including nucleation, condensation, coagulation, and deposition, have been taken into consideration in numerical studies of aerosol dynamics. Yu et al. (2008) first developed a new Taylor-series expansion method of moments (TEMOM) for the study of unimodal aerosol dynamics. Chen, Lin, and Yu (2014) developed an improved direct expansion method of moments based on the TEMOM to study nanoparticle Brownian coagulation across its entire size regime. this method provided better results for the zeroth and second order moments, when the initial geometric standard deviation is small. To extend the potential applications from unimodal to bimodal aerosol dynamics, Yu and Chan (2015) developed a new bimodal TEMOM (B-TEMOM) by constructing bimodal governing equations to solve bimodal aerosol problems. Comparing with the results obtained from the bimodal quadrature method of moments (B-QMOM) based on the QMOM by McGraw (1997) and bimodal log method of moments shows that the B-TEMOM has the capability of obtaining the first three moments and standard geometric deviations (Yu & Chan, 2015). The results of B-TEMOM in the continuum-slip regime, in which Brownian coagulation processes occur, indicates that this is a reliable method for resolving bimodal aerosol dynamics. In addition, the extension of this B-TEMOM model scheme also provides valuable foundation to the establishment of bivariate or multivariate TEMOM model scheme for solving complex aerosol related problems.

In the present numerical study, nucleation, coagulation, and condensation processes of vehicle exhaust particles were investigated. The nucleation mode adopted was binary homogeneous nucleation of a water–sulfuric acid system, parametrized for use in exhaust particle models by Vehkamaki, Kulmala, Lehtinen, and Noppel (2003). Coagulation rates were calculated with the coagulation kernels used in Yu and Chan (2015). In addition, condensation of vehicle exhaust particles was included. The present study embraces two novel aspects. First, the vehicle exhaust and the background particles are initially divided into two independent log-normal distributions, which are considered simultaneously. In previous studies (Jeong & Choi, 2005; Mueller, Blanquart, & Pitsch, 2009; Yu & Chan, 2015), only bimodal coagulation had been considered, which did not incorporate interaction between vehicle exhaust particles and background particles. Second, a coupled computational fluid dynamics (CFD)–B-TEMOM method was used, in which both two-dimensional (2-D) and three-dimensional (3-D) simulations were carried out to determine temporal and spatial evolution of vehicle exhaust particles in the environment. Thus, this newly proposed coupled CFD–B-TEMOM method provides new insight into the formation and evolution of vehicle exhaust particles, because it independently considers the effect of background particles.

2. Numerical methodology

Both 2-D and 3-D numerical models were selected to simulate the evolution of vehicle exhaust particles. The computational grid meshes used in these numerical models are shown in Fig. 1. The formation and evolution of vehicle exhaust particles in atmospheric air were investigated in simulations with varying tailpipe exit velocity, sulfur content, and relative humidity. In addition, the diameter and length of the computational domain were increased from 0.4 to 20 m and from 2 to 60 m, respectively, to obtain more far-field information from the vehicle tailpipe exit. By applying the 3-D model, detailed information about vehicle exhaust particles in radial directions was obtained. The main parameters of the 2-D and 3-D numerical models are listed in Table 1.

Fig. 1, Table 1

Grid independence and the suitability of the grid size for convergence were tested for both 2-D and 3-D numerical models. Three grid meshes with 60,000, 86,000, and 120,000 cells were used to carry out the grid independence tests for the 2-D jet stream case. The first layer of the grid near the wall was set to $y+ < 1$ for all tests. By comparing flow velocity distributions along the jet stream centerline, it was found that the relative error among these meshes was below 1%. Hence, a grid mesh of 86,000 cells was selected, as satisfying the requirements of the present 2-D numerical study and having sufficient computational accuracy and efficiency. Grid meshes with 400,000, 536,300, and 600,000 cells were used to carry out grid independence tests for the 3-D jet stream case. The flow velocity distributions along the jet stream centerline were compared, yielding a relative error among the three grids of below 2%. Therefore, taking into account both computational accuracy and efficiency, 2-D and 3-D numerical models of 86,000 and 536,300 cells were selected for the present study.

The evolution of nucleated vehicle exhaust particles in the flow field was simulated using a large eddy simulation (LES) and a bimodal Taylor-series expansion method of moments (B-TEMOM), both of which were presented in the previous work (Yu, Lin, & Chan, 2009; Yu & Chan, 2015). The simulations using the 3-D numerical model were carried out using the LES model, while a k–ε Reynolds averaged Navier–Stokes (RANS) model was used to obtain the time-averaged particle field in the 2-D numerical model. The same vehicle tailpipe exit condition, with a diameter (D_p) of 60 mm and a length (L_p) of 70 mm, was used for both the 2-D and 3-D numerical models. Boundary conditions at the inlet were fixed velocity and temperature values, while the outlet boundary had a fixed outflow.

The nucleation model used for the vehicle exhaust particles was the binary homogeneous nucleation model of water–sulfuric acid vapors proposed by Vehkamaki et al. (2003). The Kelvin effect on the aerosol evaporation rate (Friedlander, 2000) was considered in the particle condensation growth model. The growth rate of particles was obtained by considering the gain and loss of sulfuric acid molecules on the particle surface. However, the B-TEMOM (Yu & Chan, 2015; Chan et al., 2018) was used as the coagulation model. In the B-TEMOM method, the whole bimodal particle size distribution was divided into two independent log-normal distributions, each with its own independent population balance equation (PBE). The PBEs were solved using the B-TEMOM (Yu & Chan, 2015), which considers the interaction between larger background particles (Mode 1) and smaller vehicle exhaust particles (Mode 2). The PBEs of the particle field based on these two modes are given by:

$$\frac{dm_k}{dt}+\frac{\partial\left(u_j+u_{\mathrm{th}j}\right)m_k}{\partial x_j}-\frac{\partial}{\partial x_j}\left(\Gamma\frac{\partial m_k}{\partial x_j}\right)=\underbrace{\frac{1}{2}\int_0^\infty\int_0^\infty\left[(v+v')^k-v^k-v'^k\right]\beta(v,v')n(v,t)n(v',t)dvdv'}_{\text{within Mode 1}}$$
$$+\underbrace{\int_0^\infty\int_0^\infty\left[(v+v')^k-v^k\right]\beta(v,v')n(v,t)p(v',t)dvdv'}_{\text{between Mode 1 and Mode 2}}+kB_1\eta m_{k-1/3}\alpha, \quad (1)$$

$$\frac{dl_k}{dt}+\frac{\partial(u_j+u_{\mathrm{th}j})l_k}{\partial x_j}-\frac{\partial}{\partial x_j}\left(\Gamma\frac{\partial l_k}{\partial x_j}\right)=\underbrace{\frac{1}{2}\int_0^\infty\int_0^\infty[(v+v')^k-v^k-v'^k]\beta(v,v')p(v,t)p(v',t)dvdv'}_{\text{within Mode 2}}$$
$$-\underbrace{\int_0^\infty\int_0^\infty v'^k_c\beta(v,v')p(v',t)n(v,t)dvdv'}_{\text{between Mode 1 and Mode 2}}+J(v^*)v^{*k}+kB_1\eta l_{k-1/3}\alpha, \quad (2)$$

$$m_k=\int_0^\infty v^k n(v)dv, \quad (3)$$

$$l_k=\int_0^\infty v^k p(v)dv, \quad (4)$$

where in Eq. (1): $n(v,t)dv$ is the particle number density in Mode 1 having a volume of v; $p(v',t)$ is the particle number with volume v' in Mode 2; $k = 0, 1, 2 ...$; u is the fluid velocity; u_{th} is the velocity of thermophoresis; Γ is the diffusion coefficient; and $\beta(v,v')$ is the collision kernel between two particles, with volumes of v and v'. Meanwhile, n Eq. (2), $p(v,t)$ is the particle number concentration for a volume of v; J

is the nucleation rate; v^* is the volume of a critical cluster in the nucleation model; B_1 is the condensation coefficient, which is related to temperature; η is the non-dimensional concentration of sulfuric acid molecules; α is the coefficient which reflects the effect of water and hydrate on particle growth; u_{th} is the velocity of particles in thermophoresis; m_k and l_k are the k-th order moments with respect to the particle number density, $n(v)$ and $p(v)$. The first and second terms on the right-hand side of Eq. (1) represent the changes in particle number having a volume of v' related to intra-coagulation within Mode 1, and inter-particle collisions between Mode 1 and Mode 2, respectively. Similarly, the first and second terms on the right-hand side of Eq. (2) account for the particle number changes related to intra-coagulation in Mode 2 and inter-particle collisions between Mode 1 and Mode 2, respectively. The transport equations of the first three moments are outline in Eq. (A1) in the Appendix.

To achieve closure of the ordinary differential equations of moments, the fractal order must be transformed into an integer order moment. By introducing the Taylor-series expansion, the relevant closure equations can be expressed as:

$$m_k=\left(\frac{u_{\mathrm{m}}^{k-2}k^2}{2}-\frac{u_{\mathrm{m}}^{k-2}k}{2}\right)m_2+\left(-u_{\mathrm{m}}^{k-1}k^2+2u_{\mathrm{m}}^{k-1}k\right)m_1+\left(u_{\mathrm{m}}^{k}+\frac{u_{\mathrm{m}}^{k}k^2}{2}-\frac{3u_{\mathrm{m}}^{k}k}{2}\right)m_0, \tag{5}$$

$$l_k=\left(\frac{u_{\mathrm{l}}^{k-2}k^2}{2}-\frac{u_{\mathrm{l}}^{k-2}k}{2}\right)l_2+\left(-u_{\mathrm{l}}^{k-1}k^2+2u_{\mathrm{l}}^{k-1}k\right)l_1+\left(u_{\mathrm{l}}^{k}+\frac{u_{\mathrm{l}}^{k}k^2}{2}-\frac{3u_{\mathrm{l}}^{k}k}{2}\right)l_0, \tag{6}$$

where u_{m} and u_{l} represent the Taylor-expansion points of different modes. In the present study, the Taylor-expansion point is the same as that determined by Yu and Chan (2015) for Mode 1 (i.e., $u_{\mathrm{m}}=m_1/m_0$) and for Mode 2 (i.e., $u_{\mathrm{l}}=l_1/l_0$).

The dimensionless equations of the sulfuric acid molar concentration in background and exhaust particles are:

$$\frac{\partial\eta}{\partial t^*}=R^*-J^*(v^*)k^*-M_{2/3}^*\eta, \tag{7a}$$

$$\frac{\partial\eta}{\partial t^*}=R^*-J^*(v^*)k^*-L_{2/3}^*\eta, \tag{7b}$$

where η represents the concentration of sulfuric acid, $R^*=R/(n_{\mathrm{s}}/\tau)$ is the particle generation rate and k^* is the number of sulfuric acid-containing critical particles. $M_{2/3}^*$ and $L_{2/3}^*$ are dimensionless fractional moments. The dimensionless solution is identical to that of Pratsinis (1988). The dimensionless moment transport equations are given in Eq. (A2) in the Appendix.

For each mode, the first three moments have the following relationships:

$$
\begin{aligned}
N_{\mathrm{m}} &= M_0 & N_{\mathrm{l}} &= L_0 \\
D_{\mathrm{mg}} &= \frac{M_1^2}{M_0^{3/2} M_2^{1/2}} & D_{\mathrm{lg}} &= \frac{L_1^2}{L_0^{3/2} L_2^{1/2}} \\
\ln^2 \sigma_{\mathrm{mg}} &= \frac{1}{9} \ln \frac{M_0 M_2}{M_1^2} & \ln^2 \sigma_{\mathrm{lg}} &= \frac{1}{9} \ln \frac{L_0 L_2}{L_1^2}
\end{aligned} \tag{8}
$$

where D is the geometric mean diameter of the particles, N is the particle concentration, and σ is the geometric standard deviation. Through solving the first three moments, N, D, and σ can be obtained, respectively. Here, the first three order moments were used as described in Yu et al. (2008) and Yu and Lin (2009a).

3. Results and discussion

3.1. Instantaneous contours of the particle field

The instantaneous contours of the zeroth order moments and the average diameter of background particles and vehicle exhaust particles at different times are shown in Fig. 2. Over time, the concentration of background particles (M_0) near the tailpipe exit is lower, with vehicle exhaust particles mainly occurring in the jet shear layer, consistent with numerical simulation results of Yu and Lin (2009a). This affects entrainment of particles caused by the coherent structure of the jet stream (Lin et al., 2007). Compared with the concentrations of vehicle exhaust particles (L_0), background particle concentrations are much lower. With continuous entry of background particles into the aerosol mixture consisting of background and vehicle exhaust particles, the number concentration of background particles (M_0) increases accordingly (Fig. 2). Thus, the average diameter of background particles (d_{BP}) decreases rapidly, despite coagulation between background and vehicle exhaust particles. The number concentration of vehicle exhaust particles also increases with time, as new vehicle exhaust particles are formed through binary homogeneous nucleation of the water–sulfuric acid system. The average diameter of vehicle exhaust particles (d_{EP}) increases with time as coagulation occurs amongst vehicle exhaust particles, as well as ongoing condensation of gaseous species on the surfaces of vehicle exhaust particles. Background particles clearly have a much larger average diameter than vehicle exhaust particles, showing the importance of independently assessing the generated particle types.

Fig. 2

Typical concentration distributions of background and vehicle exhaust particles in plane YZ with $Z = 0$ m and $X \leq 1$ m, when evolution time, $t = 0.6$ s, are shown in Fig. 3. The numerical simulation results obtained with the B-TEMOM model scheme were verified against those obtained using the moving sectional method (MSM) (Tsantilis, Kammler, & Pratsinis, 2002) and the B-QMOM with four Gaussian quadrature points (McGraw, 1997); these models were also used in Chan et al. (2018), and Yu and Chan (2015), respectively. Excellent agreements between the B-TEMOM and both the MSM and the B-QMOM were obtained.

Compared with the MSM and the B-QMOM, the B-TEMOM is a relatively simple algorithm, with high computational accuracy and efficiency in obtaining moments of particles. In all studied numerical models, the centerline of the tailpipe exit lies at $Y = 0$ m; therefore, a larger Y value represents a larger distance from the centerline of the tailpipe exit. The positive direction of the X axis is in the jet flow direction; therefore, larger X values are farther from the tailpipe exit. L_0 shows the concentration distribution of vehicle exhaust particles within the YZ plane. The number concentration of vehicle exhaust particles increases with increasing X. This may be because the coagulation effect decreases, while the nucleation process becomes dominant with increasing X. When $t = 0.6$ s, the two symmetrical L_0 peaks gradually disappear with increasing X, which implies that the distribution of vehicle exhaust particles becomes more stable as particles move along the jet flow direction. The concentration distribution of background particles M_0 along the axial direction increases with time. However, two opposing trends in the concentration of background particles were observed when $t = 0.6$ s. At first, the concentration of background particles increases with increasing X, when the radial distance (Y) is smaller than 0.02 m. However, when Y is larger than 0.02 m, the concentration of background particles decreases with the increasing X. These changes in concentration of the background particles may be explained by mixing caused by turbulent diffusion (Yu, Lin, & Chen, 2007). When Y is small ($Y < 0.02$ m), the number of background particles entrained by the continuous fluid is very small within the jet stream core region. Behavior of background particles within the jet stream core is mainly governed by turbulent diffusion of surrounding aerosol particles. The number concentration increases with increasing X within this core region, as more background particles are entrained as X becomes larger. However, for the region with $Y > 0.02$ m, which is farther from the jet stream potential core, the background particles are entrained into the jet stream by turbulent diffusion. Thus, when $Y > 0.02$ m, M_0 decreases with increasing X. Because the concentration of background particles is not very high ($< 10^{10}$ #/m^3) in the present study, the effect of coagulation is not observed in these simulations.

3.2. Time-averaged particle field

3.2.1. Effect of background particles

The lognormal distributions of particles at various locations in China were selected to represent the distributions of background particles (i.e., particles in the surrounding environment) in the numerical simulations. Table 2 shows the simulated parameters of lognormal modes for the distributions of background particle number size at these various locations in China (Wu et al., 2008; Peng et al., 2014), as well as the typical physical properties and formation mechanisms of these background particles. Fig. 4 shows the simulated time-averaged particle concentration distributions at different positions along the axis of the exhaust tailpipe. The distributions of L_0 and d_{EP} show that the impact of the concentration and diameter of background particles on the vehicle exhaust particles can be neglected, if the same temperature and the concentration of background particles are set within the studied range. However, if the background particles are removed completely from the simulation, then vehicle exhaust particles have lower number concentrations and larger average diameters, indicating that higher concentrations and smaller average

diameters of vehicle exhaust particles are highly related to the impact of background particles on nucleation, coagulation, and condensation processes . An enlarged view of the exhaust tailpipe outlet shows that the lower the concentration of background particles, the larger the distance from the tailpipe exit at which the average diameter of these background particles reaches a steady-state value. This implies that there is a larger impact of vehicle exhaust particles on background particles at low particle number concentrations.

Table 2, Fig. 4

3.2.2. Effect of tailpipe exit velocity on the total particle number concentration

The concentration distributions and geometric average diameters of background particles and vehicle exhaust particles along the axial direction X for different tailpipe exit velocities is shown in Fig. 5. According to the variation of the number concentration of background particles (i.e., M_0), the critical axial distance increases with increasing tailpipe exit velocity. The critical axial distance is defined herein as the position at which the particle concentration varies significantly. These results are consistent with the fact that particles are mainly distributed within the boundary region of the exhaust jet stream. A larger tailpipe exit velocity produces a larger exhaust jet flow region, having a larger distance between the exhaust jet stream boundary and the tailpipe outlet. Thus, higher tailpipe exit velocity causes lower steady-state concentrations and larger geometric average diameters of vehicle exhaust particles, because a higher tailpipe exit velocity causes a larger gradient in velocity and higher coagulation of vehicle exhaust particles takes place. Coagulation typically produces lower concentrations and larger geometric average diameters of vehicle exhaust particles. However, Fig. 5 shows that the tailpipe exit velocity has little effect on the geometric average diameter of background particlesd_{BP}. This may be because of the lower number concentrations of background particles ($< 10^{10}$ #/m^3) compared with vehicle exhaust particles ($> 10^{13}$ #/m^3), which results in negligible coagulation of background particles. This implies that increasing the tailpipe exit velocity does not significantly affect the average diameter of background particles.

Fig. 5

3.2.3. Effect of sulfur content

The effect of sulfur content on the distribution of background and vehicle exhaust particles along axial direction X is shown in Fig. 6. These results are consistent with simulation cases that only consider a mono-normal distribution (Yu et al., 2009). With increasing sulfur content, both the geometric average diameter and the concentration of exhaust particles at steady-state increase. Unlike effects of tailpipe exit velocity and relative humidity, sulfur content not only impacts on the concentration and diameter of vehicle exhaust particles but also changes the geometric average diameter of the background particles. This suggests that sulfur species serve as reactants during the evolution of vehicle exhaust particles and during the growth of background particles. However, sulfur content had almost no effect on the number concentration of

background particles as shown in Fig. 6,, suggesting that sulfur had no effect on coagulation processes of background particles in the presemt study.

Fig. 6

3.2.4. Effect of ambient relative humidity

The effect of ambient relative humidity on the distribution of particles along the axial direction X is shown in Fig. 7. These results show that under higher ambient relative humidity, the nucleation rate is higher, yielding smaller average diameters of vehicle exhaust particles, as reported in a previous study (Yu et al., 2009). Because the nucleated particles are small, ambient relative humidity only slightly impacts on the number concentration of vehicle exhaust particles. Its impact on background particles also is not significant**.** The effect of ambient relative humidity on the nucleation rate is shown in Fig. 8. This effect is more significant when the axial distance is smaller than 5 m. Results shown in Figs. 7 and 8 suggest that ambient relative humidity only has a slight effect on number concentrations and geometric average diameters during the initial stages of particle evolution.

Figs. 7 & 8

4. Conclusions

A bimodal Taylor expansion method of moments (B-TEMOM) model scheme for simulating bimodal aerosol dynamics was developed and verified against the moving sectional method (Tsantilis et al., 2002) and bimodal quadrature method of moments (modified after McGraw, 1997). A coupled of B-TEMOM and LES/k–ε RANS numerical model was used for simulation of aerosol dynamics under varying background particles , tailpipe exit velocities, sulfur contents, and ambient relative humidities. Results showed that addition of background particles to the surrounding environment caused higher concentration and smaller geometric average diameter of vehicle exhaust particles. Tailpipe exit velocity and ambient relative humidity had the least effect on the steady-state concentration and average diameter of background particles, while sulfur content affected the average diameter of background particles but had no noticeable effect on particle concentrations. In this case, higher sulfur content generated larger geometric average diameters of background particles. The effects of studied parameters on the vehicle exhaust particles were consistent with previous work, which only considered mono-logarithmic distributions of particles (Yu et al., 2009). This coupled CFD-B-TEMOM numerical model provides a simple but accurate and efficient method for studying bimodal aerosol dynamics.

Acknowledgements

This work was supported by the grants from the General Research Fund, Research Grants Council of the Hong Kong Special Administrative Region, China (Project Nos. PolyU 5101/13E and PolyU 152125/15E)),

and the Central Research Grant of The Hong Kong Polytechnic University (Project Nos. B-Q39E and B-Q47Y). The financial support is greatly appreciated for the further development and extension of the Bimodal TEMOM model scheme, and the establishment of a novel Bivariate TEMOM model scheme.

Appendix

A1. Transport equations of the first three moments

After transformation, the moment transport equations (i.e., Eqs (1) and (2)) can be expressed as differential equations of moments with different orders. If only three moments are considered, then Eqs. (1) and (2) can be expressed as:

$$
\begin{aligned}
\frac{dm_0}{d(B_2 t)} &= -\frac{\partial(u_j+u_{\mathrm{th}j})m_0}{\partial x_j}+\frac{\partial}{\partial x_j}\left(\Gamma\frac{\partial m_0}{\partial x_j}\right)-\frac{1}{2}\left[{\xi_1}^{*}+\emptyset v_{\mathrm{p}0}^{f-\frac{1}{3}}{\xi_2}^{*}\right]\\
\frac{dm_1}{d(B_2 t)} &= -\frac{\partial(u_j+u_{\mathrm{th}j})m_1}{\partial x_j}+\frac{\partial}{\partial x_j}\left(\Gamma\frac{\partial m_1}{\partial x_j}\right)+\left[{\eta_1}^{**}+\emptyset v_{\mathrm{p}0}^{f-\frac{1}{3}}{\eta_2}^{**}\right]+\left(\frac{B_1}{B_2}\right)\\
\frac{dm_2}{d(B_2 t)} &= -\frac{\partial(u_j+u_{\mathrm{th}j})m_2}{\partial x_j}+\frac{\partial}{\partial x_j}\left(\Gamma\frac{\partial m_2}{\partial x_j}\right)+\frac{1}{2}\left[{\zeta_1}^{*}+\emptyset v_{\mathrm{p}0}^{f-\frac{1}{3}}{\zeta_2}^{*}\right]\\
&\quad+\left[{\vartheta_1}^{**}+{\vartheta_2}^{**}\emptyset v_{\mathrm{p}0}^{f-\frac{1}{3}}\right]+2\left(\frac{B_1}{B_2}\right)\eta m_{5/3}\alpha\\
\frac{dl_0}{d(B_2 t)} &= -\frac{\partial(u_j+u_{\mathrm{th}j})l_0}{\partial x_j}+\frac{\partial}{\partial x_j}\left(\Gamma\frac{\partial l_0}{\partial x_j}\right)-\frac{1}{2}\left[{\xi_1}^{*'}+\emptyset v_{\mathrm{p}0}^{f-\frac{1}{3}}{\xi_2}^{*'}\right]\\
&\quad-\left[{\xi_1}^{**}+\emptyset v_{\mathrm{p}0}^{f-\frac{1}{3}}{\xi_2}^{**}\right]+J(v^{*})\\
\frac{dl_1}{d(B_2 t)} &= -\frac{\partial(u_j+u_{\mathrm{th}j})l_1}{\partial x_j}+\frac{\partial}{\partial x_j}\left(\Gamma\frac{\partial l_1}{\partial x_j}\right)-\left[{\eta_1}^{**}+\emptyset v_{\mathrm{p}0}^{f-\frac{1}{3}}{\eta_2}^{**}\right]\\
&\quad-\left[{\xi_1}^{**}+\emptyset v_{\mathrm{p}0}^{f-\frac{1}{3}}{\xi_2}^{**}\right]+J(v^{*})\\
\frac{dl_2}{d(B_2 t)} &= -\frac{\partial(u_j+u_{\mathrm{th}j})l_2}{\partial x_j}+\frac{\partial}{\partial x_j}\left(\Gamma\frac{\partial l_2}{\partial x_j}\right)+\frac{1}{2}\left[{\zeta_1}^{*'}+\emptyset v_{\mathrm{p}0}^{f-\frac{1}{3}}{\zeta_2}^{*'}\right]\\
&\quad-\left[{\varsigma_1}^{**}+{\varsigma_2}^{**}\emptyset v_{\mathrm{p}0}^{f-\frac{1}{3}}\right]+J(v^{*})\left(\frac{v^{*}}{v_w}\right)^{2}\alpha+2\left(\frac{B_1}{B_2}\right)\eta l_{5/3}
\end{aligned}
\tag{A1}
$$

with

$$
\begin{aligned}
{\xi_1}^{*} &= 2m_0 m_0+m_{\mathrm{f}}\,m_{-\mathrm{f}}+m_{-\mathrm{f}}\,m_{\mathrm{f}}\\
{\xi_2}^{*} &= m_0 m_{-\mathrm{f}}+m_{\mathrm{f}}\,m_{-2\mathrm{f}}+m_{\mathrm{f}}\,m_{-2\mathrm{f}}+m_0 m_{-\mathrm{f}}\\
{\xi_1}^{*'} &= 2l_0 l_0+l_{\mathrm{f}}\,l_{-\mathrm{f}}+l_{-\mathrm{f}}\,l_{\mathrm{f}}\\
{\xi_2}^{*'} &= l_0\,l_{-\mathrm{f}}+l_{\mathrm{f}}\,l_{-2\mathrm{f}}+l_{\mathrm{f}}\,l_{-2\mathrm{f}}+l_0\,l_{-\mathrm{f}}\\
{\xi_1}^{**} &= 2m_0 l_0+m_{\mathrm{f}}\,l_{-\mathrm{f}}+m_{-\mathrm{f}}\,l_{\mathrm{f}}\\
{\xi_2}^{**} &= m_0 l_{-\mathrm{f}}+m_{\mathrm{f}}l_{-2\mathrm{f}}+l_{\mathrm{f}}\,m_{-2\mathrm{f}}+l_0 m_{-\mathrm{f}}
\end{aligned}
$$

$$\eta_1^{**} = 2m_0 l_1 + m_f\, l_{-f+1} + m_{-f}\, l_{f+1}$$

$$\eta_2^{**} = m_{-f} l_1 + m_f l_{-2f+1} + m_{-2f} l_{f+1} + m_0 l_{-f+1}$$

$$\zeta_1^{*} = 4m_1 m_1 + 2m_{1+f} m_{1-f} + 2m_{1+f} m_{1-f}$$

$$\zeta_2^{*} = 2m_{1-f} m_1 + 2m_{1+f} m_{1-2f} + 2m_{1-2f} m_{1+f} + 2m_1 m_{1-f}$$

$$\zeta_1^{*\prime} = 4l_1 l_1 + 2l_{1+f} l_{1-f} + 2l_{1+f} l_{1-f}$$

$$\zeta_2^{*\prime} = 2l_{1-f} l_1 + 2l_{1+f} l_{1-2f} + 2l_{1-2f} l_{1+f} + 2l_1 l_{1-f}$$

$$\zeta_1^{**} = 4m_1 l_1 + 2m_{1+f} l_{1-f} + 2m_{1-f} l_{1+f}$$

$$\zeta_2^{**} = 2m_{1-f} l_1 + 2m_{1-2f} l_{1+f} + 2m_{1+f} l_{1-2f} + 2m_1 l_{1-f}$$

$$\varsigma_1^{**} = 2m_0 l_2 + m_f l_{2-f} + m_{-f} l_{f+2}$$

$$\varsigma_2^{**} = m_{-f} l_2 + m_f l_{2-2f} + m_{-2f} l_{2+f} + m_0 l_{2-f}$$

$$\vartheta_1^{**} = \varsigma_1^{**} + \zeta_1^{**}$$

$$\vartheta_2^{**} = \varsigma_2^{**} + \zeta_2^{**}$$

A2. Non-dimensionalization of the moment transport equations

If the dimensionalized moment transport equations are used, then numerical uncertainty usually occurs because of extremely large differences in values of traced moments. To overcome this shortcoming of dimensionalized moment equations, non-dimensionalized moment equations are implemented. The non-dimensionalization method used in the present study is modified after Pratsinis (1988); all non-dimensional terms are listed in Table A1. The coagulation rates are calculated using the same bimodal method approach described in Yu and Chan (2015).

Table A1 Non-dimensional terms used in the present study

Term	Meaning
$\tau = 1/[n_s s_1 (k_b T/2\pi m_a)^{1/2}]$	Characteristic time where s_1 is the surface area of sulfuric acid molecule, n_s is the reference concentration of sulfuric acid molecule in gas phase, m_a is the molecular mass of sulfuric acid.
$t^* = t/\tau$	Dimensionless time
$m_k^* = m_k / n_s v_a^k$ $l_k^* = l_k / n_s v_a^k$	Dimensionless k-th order moment where v_a is the volume of sulfuric acid molecule, $v_a = v_{p0}$.
$J^*(v^*) = \frac{J(v^*)}{n_s/\tau}$	Dimensionless nucleation rate
k^*	Number of sulfuric acid molecule in critical cluster
R^*	Production rate of particles from the gas phase

Based on the non-dimensional terms in Table A1, the dimensionless moment equations for the particle field are given by:

$$
\begin{aligned}
&\frac{dm_0^*}{d(B_2 t)} = -\frac{1}{2} n_s \left[\left(\xi_1^{*}\right)^{*} + \emptyset v_{p0}^{-\frac{1}{3}} \left(\xi_2^{*}\right)^{*} \right] \\
&\frac{dm_1^*}{d(B_2 t)} = n_s \left[\left(\eta_1^{**}\right)^{*} + \emptyset v_{p0}^{-\frac{1}{3}} \left(\eta_2^{**}\right)^{*} \right] \\
&\frac{dm_2^*}{d(B_2 t)} = \frac{1}{2} n_s \left[\left(\zeta_1^{*}\right)^{*} + \emptyset v_{p0}^{-\frac{1}{3}} \left(\zeta_2^{*}\right)^{*} \right] + n_s \left[\left(\vartheta_1^{**}\right)^{*} + \left(\vartheta_2^{**}\right)^{*} \emptyset v_{p0}^{-\frac{1}{3}} \right] \\
&\frac{dl_0^*}{d(B_2 t)} = J^*\left(v^*\right) - \frac{1}{2} n_s \left[\left(\xi_1^{*'}\right)^{*} + \emptyset v_{p0}^{-\frac{1}{3}} \left(\xi_2^{*'}\right)^{*} \right] - n_s \left[\left(\xi_1^{**}\right)^{*} + \emptyset v_{p0}^{-\frac{1}{3}} \left(\xi_2^{**}\right)^{*} \right] \\
&\frac{dl_1^*}{\mathrm{d}(B_2 t)} = J^*\left(v^*\right) \frac{v^*}{v_{p0}} + \left(\frac{B_1}{B_2}\right) \eta l_{2/3}^* \alpha - n_s \left[\left(\eta_1^{**}\right)^{*} + \emptyset v_{p0}^{-\frac{1}{3}} \left(\eta_2^{**}\right)^{*} \right] \\
&\frac{dl_2^*}{d(B_2 t)} = J^*\left(v^*\right) \left(\frac{v^*}{v_{p0}}\right)^2 + 2\left(\frac{B_1}{B_2}\right) \eta l_{5/3}^* \alpha + \frac{1}{2} n_s \left[\left(\zeta_1^{*'}\right)^{*} + \emptyset v_{p0}^{-\frac{1}{3}} \left(\zeta_2^{*'}\right)^{*} \right] - n_s \left[\left(\varsigma_1^{**}\right)^{*} + \left(\varsigma_2^{**}\right)^{*} \emptyset v_{p0}^{-\frac{1}{3}} \right]
\end{aligned}
\tag{A2}
$$

where:

$$
\begin{aligned}
\left(\xi_1^{**}\right)^{*} &= 2m_0^* l_0^* + m_f^* l_{-f}^* + m_{-f}^* l_f^* \\
\left(\xi_2^{**}\right)^{*} &= m_0^* l_{-f}^* + m_f^* l_{-2f}^* + l_f^* m_{-2f}^* + l_0^* m_{-f}^* \\
\left(\eta_1^{**}\right)^{*} &= 2m_0^* l_1^* + m_f^* l_{1-f}^* + m_{-f}^* l_{1+f}^* \\
\left(\eta_2^{**}\right)^{*} &= m_{-f}^* l_1^* + m_f^* l_{1-2f}^* + m_{-2f}^* l_{1+f}^* + m_0^* l_{1-f}^* \\
\left(\zeta_1^{*}\right)^{*} &= 4m_1^* m_1^* + 2m_{1+f}^* m_{1-f}^* + 2m_{1+f}^* m_{1-f}^* \\
\left(\zeta_2^{*}\right)^{*} &= 2m_{1-f}^* m_1^* + 2m_{1+f}^* m_{1-2f}^* + 2m_{1-2f}^* m_{1+f}^* + 2m_1^* m_{1-f}^* \\
\left(\zeta_1^{*'}\right)^{*} &= 4l_1^* l_1^* + 2l_{1+f}^* l_{1-f}^* + 2l_{1+f}^* l_{1-f}^* \\
\left(\zeta_2^{*'}\right)^{*} &= 2l_{1-f}^* l_1^* + 2l_{1+f}^* l_{1-2f}^* + 2l_{1-2f}^* l_{1+f}^* + 2l_1^* l_{1-f}^* \\
\left(\varsigma_1^{**}\right)^{*} &= 2m_0^* l_2^* + m_f^* l_{2-f}^* + m_{-f}^* l_{2+f}^* \\
\left(\varsigma_2^{**}\right)^{*} &= m_{-f}^* l_2^* + m_f^* l_{2-2f}^* + m_{-2f}^* l_{2+f}^* + m_0^* l_{2-f}^* \\
\left(\zeta_1^{**}\right)^{*} &= 4m_1^* l_1^* + 2m_{1+f}^* l_{1-f}^* + 2m_{1-f}^* l_{1+f}^* \\
\left(\zeta_2^{**}\right)^{*} &= 2m_{1-f}^* l_1^* + 2m_{1-2f}^* l_{1+f}^* + 2m_{1+f}^* l_{1-2f}^* + 2m_1^* l_{1-f}^* \\
\left(\vartheta_1^{**}\right)^{*} &= \left(\varsigma_1^{**}\right)^{*} + \left(\zeta_1^{**}\right)^{*} \\
\left(\vartheta_2^{**}\right)^{*} &= \left(\varsigma_2^{**}\right)^{*} + \left(\zeta_2^{**}\right)^{*}
\end{aligned}
$$

References

Alam, M.S., Zeraati-Rezaei, S., Stark, C.P., Liang, Z.R., Xu, H.M., & Harrison, R.M. (2016). The characterisation of diesel exhaust particles-composition, size distribution and partitioning. *Faraday Discussions*, 189, 69-84.

Araujo, J.A., & Nel, A.E. (2009). Particulate matter and atherosclerosis: Role of particle size, composition and oxidative stress. *Particle and Fibre Toxicology*, *6*, 24.

Asmi, A., Wiedensohler, A., Laj, P., Fjaeraa, A.-M., Sellegri, K., & Birmili, W., et al. (2011). Number size distributions and seasonality of submicron particles in Europe 2008–2009. *Atmospheric Chemistry and Physics*, *11*(11), 5505-5538.

Chan, T. L., Dong, G., Cheung, C. S., Leung, C. W., Wong, C. P., & Hung, W. T. (2001). Monte Carlo simulation of nitrogen oxides dispersion from a vehicular exhaust plume and its sensitivity studies. *Atmospheric Environment*, *35*(35), 6117-6127.

Chan, T. L., & Ning, Z. (2005). On-road remote sensing of diesel vehicle emissions measurement and emission factors estimation in Hong Kong. *Atmospheric Environment, 39*(36), 6843-6856.

Chan, T. L., Zhou, K., & Lin, J. Z. (2005, October). Modeling study of gas-to-nanoparticle conversion from a vehicular exhaust plume. In *Proceedings of International Conference on Jets, Wakes and Separated Flows, ICJWSF-2005* (Paper No. P-124, pp. 5-8). Toba-shi, Mie, Japan.

Chan, T.L., Liu, Y.H., & Chan, C.K. (2010). Direct quadrature method of moments for the exhaust particle formation and evolution in the wake of the studied ground vehicle. *Journal of Aerosol Science*, *41*(6), 553-568.

Chan, T.L., Liu, S.Y., & Yue, Y. (2018). Nanoparticle formation and growth in turbulent flows using the bimodal TEMOM. *Powder Technology*, *323*, 507-517.

Chen, Z., Lin, J., & Yu, M. (2014). Direct expansion method of moments for nanoparticle Brownian coagulation in the entire size regime. *Journal of Aerosol Science, 67*(1), 28-37.

Freutel, F., Schneider, J., Drewnick, F., von der Weiden-Reinmüller, S.-L., Crippa, M., & Prévôt, A. S. H., et al. (2013). Aerosol particle measurements at three stationary sites in the megacity of Paris during summer 2009: Meteorology and air mass origin dominate aerosol particle composition and size distribution. *Atmospheric Chemistry and Physics*, *13*(2), 933-959.

Friedlander, S. (2000). *Smoke, dust and haze: Fundamentals of aerosol dynamics* (2nd ed.). Oxford: Oxford University Press.

González, Y., & Rodríguez, S. (2013). A comparative study on the ultrafine particle episodes induced by vehicle exhaust: A crude oil refinery and ship emissions. *Atmospheric Research*, *120*(3), 43-54.

Jeong, J.I., & Choi, M. (2005). A bimodal particle dynamics model considering coagulation, coalescence and surface growth, and its application to the growth of titania aggregates. *Journal of Colloid and Interface Science, 281*(2): 351–359.

Kim, J., Jung, C. H., Choi, B. C., Oh, S. N., Brechtel, F. J., & Yoon, S. C. (2007). Number size distribution of atmospheric aerosols during ACE-Asia dust and precipitation events. *Atmospheric Environment*, *41*(23), 4841-4855.

Kim, K. H., Kabir, E., & Kabir, S. (2015). A review on the human health impact of airborne particulate matter. *Environment International*, *74*, 136-143.

Kittelson, D. B. (1998). Engines and nanoparticles: A review. *Journal of Aerosol Science*, *29*(5), 575-588.

Kittelson, D., Watts, W., Johnson, J., Thorne, C., Higham, C., & Payne, M., et al. (2008). Effect of fuel and lube oil sulfur on the performance of a diesel exhaust gas continuously regenerating trap. *Environmental Science & Technology*, *42*(24), 9276-9282.

Li, Z., Wen, Q., & Zhang, R. (2017). Sources, health effects and control strategies of indoor fine particulate matter ($PM_{2.5}$): A review. *Science of the Total Environment*, *586*, 610-622.

Lin, J.Z., Chan, T.L., Liu, S., Zhou, K., Zhou, Y., & Lee, S.C. (2007). Effects of coherent structures on nanoparticle coagulation and dispersion in a round jet. *International Journal of Nonlinear Sciences and Numerical Simulation*, *8*(1), 45-54.

Liu, H.J., Yu, M.Z., Yin, Z.Q., Jiang, Y., & Chen, M.G. (2014). Study on the evolution of nanoparticle size distribution due to continuous injection using the sectional method. *International Journal of Numerical Methods for Heat & Fluid Flow*, *24*(8), 1803-1812.

Liu, S.Y. & Chan, T.L. (2017). A coupled CFD-Monte Carlo method for simulating complex aerosol dynamics in turbulent flows. *Aerosol Science and Technology*, *51*(3), 269-281.

Liu, H.M. & Chan, T.L. (2018). A differentially weighted operator splitting Monte Carlo method for simulating complex aerosol dynamic processes. *Particuology*, 36, 114-126.

McGraw, R. (1997). Description of aerosol dynamics by the quadrature method of moments. *Aerosol Science and Technology*, *27*(2), 255-265.

Medina, R., Fitzgerald, R. M., & Min, Q. (2012). Retrieval of the single scattering albedo in the El Paso-Juarez Airshed using the TUV model and a UV-MFRSR radiometer. *Atmospheric Environment, 46*, 430-440.

Mönkkönen, P., Koponen, I. K., Lehtinen, K. E. J., Hämeri, K., Uma, R., & Kulmala, M. (2005). Measurements in a highly polluted Asian mega city: Observations of aerosol number size distribution, modal parameters and nucleation events. *Atmospheric Chemistry and Physics*, *5*(1), 57-66.

Morawska, L., & Zhang, J. J. (2002). Combustion sources of particles. 1. Health relevance and source signatures. *Chemosphere*, *49*(9), 1045-1058.

Mueller, M.E., Blanquart, G., & Pitsch, H. (2009). Hybrid method of moments for modeling soot formation and growth. *Combustion and Flame, 156*(6), 1143-1155.

Ning, Z., Chan, K. L., Wong, K. C., Westerdahl, D., Močnik, G., & Zhou, J. H. (2013). Black carbon mass size distributions of diesel exhaust and urban aerosols measured using differential mobility analyzer in tandem with Aethalometer. *Atmospheric Environment*, *80*(80), 31-40.

Olin, M., Rönkkö, T., & Dal Maso, M. (2015). CFD modeling of a vehicle exhaust laboratory sampling system: sulfur-driven nucleation and growth in diluting diesel exhaust. *Atmospheric Chemistry and Physics*, *15*(9), 5305-5323.

Pant, P., & Harrison, R. M. (2013). Estimation of the contribution of road traffic emissions to particulate matter concentrations from field measurements: A review. *Atmospheric Environment*, *77*(7), 78-97.

Peng, J. F., Hu, M., Wang, Z. B., Huang, X. F., Kumar, P., & Wu, Z. J., et al. (2014). Submicron aerosols at thirteen diversified sites in China: Size distribution, new particle formation and corresponding contribution to cloud condensation nuclei production. *Atmospheric Chemistry and Physics*, *14*(18), 10249-10265.

Pope, C. A., Burnett, R. T., Thurston, G. D., Thun, M. J., Calle, E. E., & Krewski, D., et al. (2004). Cardiovascular mortality and long-term exposure to particulate air pollution. *Circulation*, *109*(1), 71-77.

Pratsinis, S. E. (1988). Simultaneous nucleation, condensation, and coagulation in aerosol reactors. *Journal of Colloid and Interface Science*, *124*(2), 416-427.

Rönkkö, T., Virtanen, A., Kannosto, J., Keskinen, J., Lappi, M., & Pirjola, L. (2007). Nucleation mode particles with a nonvolatile core in the exhaust of a heavy duty diesel vehicle. *Environmental Science & Technology*, *41*(18), 6384-6389.

Rose, D., Nowak, A., Achtert, P., Wiedensohler, A., Hu, M., & Shao, M., et al. (2010). Cloud condensation nuclei in polluted air and biomass burning smoke near the mega-city Guangzhou, China–Part 1: Size-resolved measurements and implications for the modeling of aerosol particle hygroscopicity and CCN activity. *Atmospheric Chemistry and Physics*, *10*(7), 3365-3383.

Sun, Y., Zhou, X., & Wang, W. (2016). Aerosol size distributions during haze episodes in winter in Jinan, China. *Particuology, 28*(5), 77-85.

Tang, H., & Li, X. X. (2014). Research on the single scattering albedo of spheroids. *International Journal of Numerical Methods for Heat & Fluid Flow*, *24*(8), 1762-1768.

Tsantilis, S., Kammler, H. K., & Pratsinis, S. E. (2002). Population balance modeling of flame synthesis of titania nanoparticles. *Chemical Engineering Science, 57*(12), 2139-2156.

Tie, X., & Cao, J. (2009). Aerosol pollution in China: Present and future impact on environment. *Particuology, 7*(6), 426-431.

Vehkamäki, H., Kulmala, M., Lehtinen, K. E., & Noppel, M. (2003). Modelling binary homogeneous nucleation of water-sulfuric acid vapours: Parameterisation for high temperature emissions. *Environmental Science & Technology*, *37*(15), 3392-3398.

Wang, J.S., Chan, T.L., Cheung, C.S., Leung, C.W., & Hung, W.T. (2006). Three-dimensional pollutant concentration dispersion from a vehicular exhaust plume in the real atmosphere. *Atmospheric Environment, 40*(3), 484-497.

Wu, Z., Hu, M., Lin, P., Liu, S., Wehner, B., & Wiedensohler, A. (2008). Particle number size distribution in the urban atmosphere of Beijing, China. *Atmospheric Environment*, *42*(34), 7967-7980.

Yu, F., & Luo, G. (2009). Simulation of particle size distribution with a global aerosol model: Contribution of nucleation to aerosol and CCN number concentrations. *Atmospheric Chemistry and Physics*, *9*(20), 7691-7710.

Yu, M., Lin, J., & Chen, L. (2007). Nanoparticle coagulation in a planar jet via moment method. *Applied Mathematics and Mechanics* (English Edition), *28*(11), 1445-1453.

Yu, M., Lin, J., & Chan, T. (2008). A new moment method for solving the coagulation equation for particles in Brownian motion. *Aerosol Science and Technology*, *42*(9), 705-713.

Yu, M., Lin, J., & Chan, T. (2009). Numerical simulation for nucleated vehicle exhaust particulate matters via the TEMOM/LES method. *International Journal of Modern Physics C*, *20*(03), 399-421.

Yu, M., & Lin, J. (2009a). Taylor-expansion moment method for agglomerate coagulation due to Brownian motion in the entire size regime. *Journal of Aerosol Science*, *40*(6), 549-562.

Yu, M., & Lin, J. (2009b). Solution of the agglomerate Brownian coagulation using Taylor-expansion moment method. *Journal of Colloid and Interface Science*, *336*(1), 142-149.

Yu, M., & Lin, J. (2010). Nanoparticle-laden flows via moment method: A review. *International Journal of Multiphase Flow*, *36*(2), 144-151.

Yu, M., Lin, J., Jin, H., & Jiang, Y. (2011). The verification of the Taylor-expansion moment method for the nanoparticle coagulation in the entire size regime due to Brownian motion. *Journal of Nanoparticle*

Research, *13*(5), 2007-2020.
Yu, M.Z., & Chan, T.L. (2015). A bimodal moment method model for submicron fractal-like agglomerates undergoing Brownian coagulation. *Journal of Aerosol Science, 88,* 19-34.
Yu, M., Zhang, X., Jin, G., Lin, J., & Seipenbusch, M. (2015). A new analytical solution for solving the population balance equation in the continuum-slip regime. *Journal of Aerosol Science*, *80*, 1-10.
Yue, D.L., Hu, M., Zhang, R. Y., Wang, Z. B., Zheng, J., & Wu, Z. J., et al. (2010). The roles of sulfuric acid in new particle formation and growth in the mega-city of Beijing. *Atmospheric Chemistry and Physics*, *10*(10), 4953-4960.

Figures

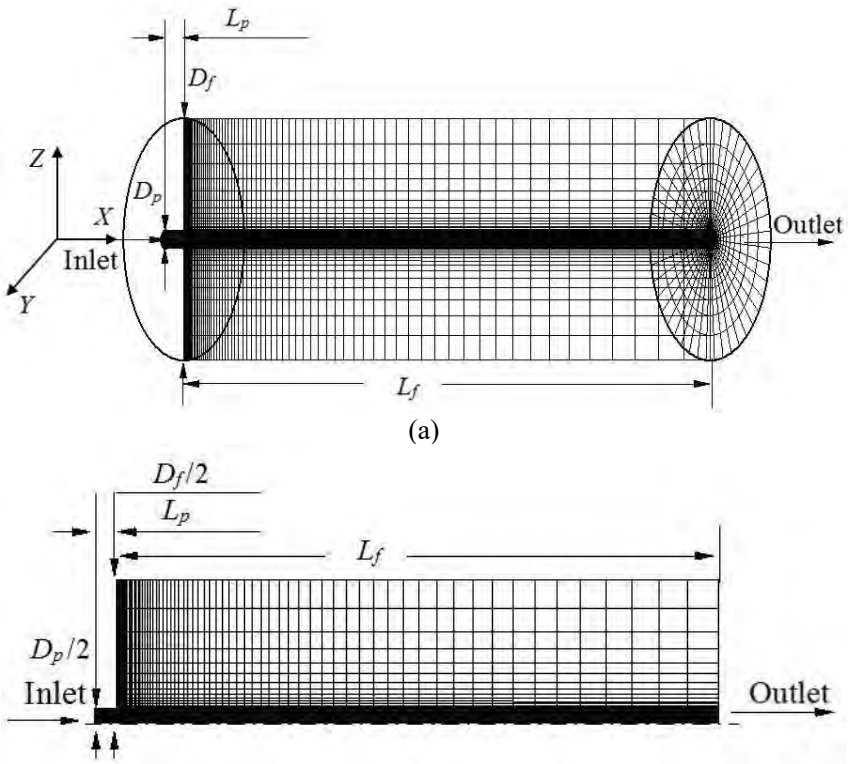

Fig. 1. Schematic figure of the computational domain for vehicle exhaust particles in (a) three-dimensional numerical model; and (b) two-dimensional numerical model. D_p and L_p are the diameter and length of the vehicle tailpipe; while D_f and L_f are the diameter and length of the far-field in the computation.

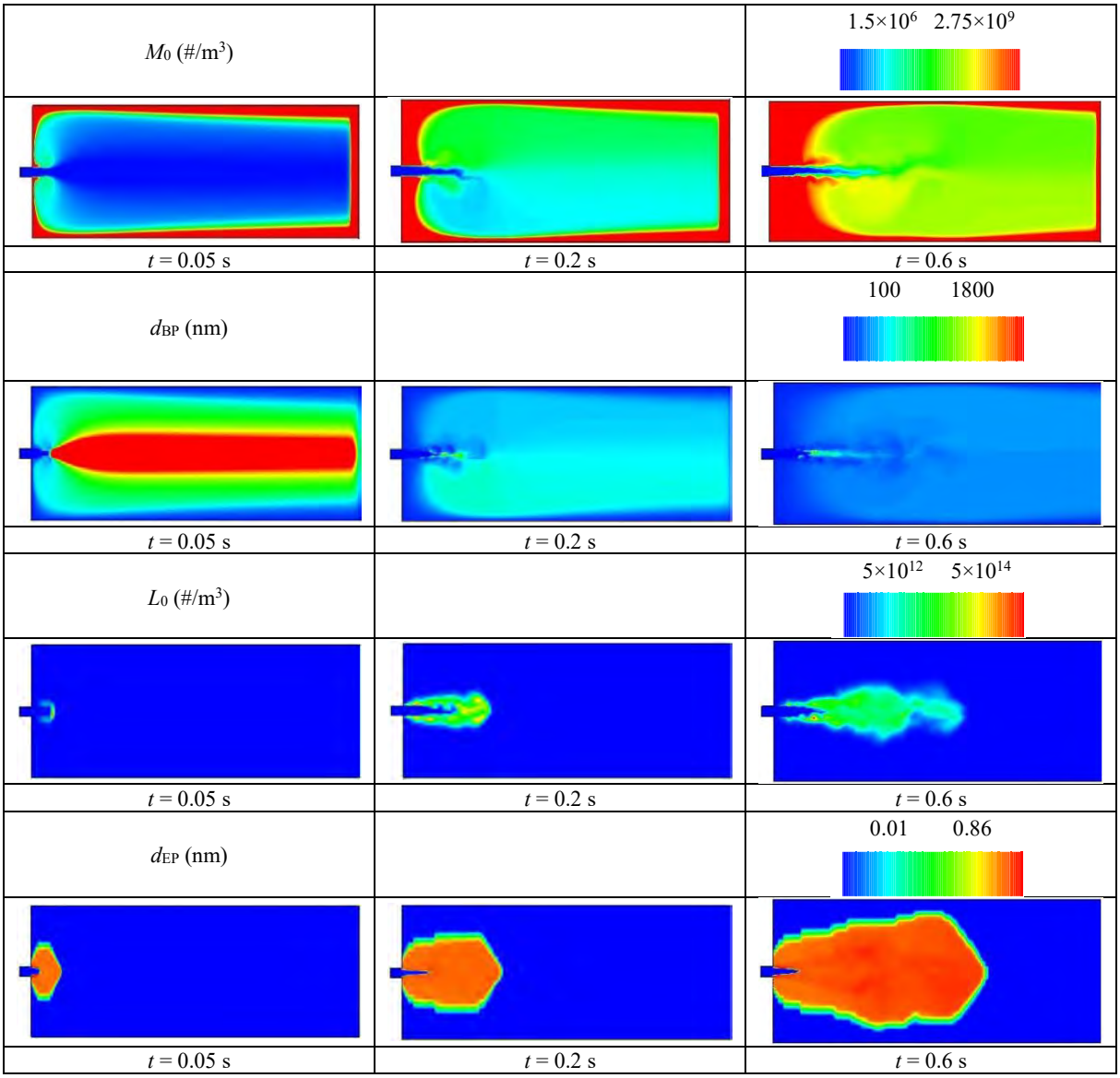

Fig. 2. Instantaneous contours of the zeroth order moments and average diameters of background and vehicle exhaust particles at different times within the XY plane at $Z = 0$. M_0 and L_0 are the zeroth order moments of background and vehicle exhaust particles, respectively; while d_{BP} and d_{EP} are the average diameters of background and vehicle exhaust particles, respectively. The parameter range in each figure is indicated above the gradient color bar.

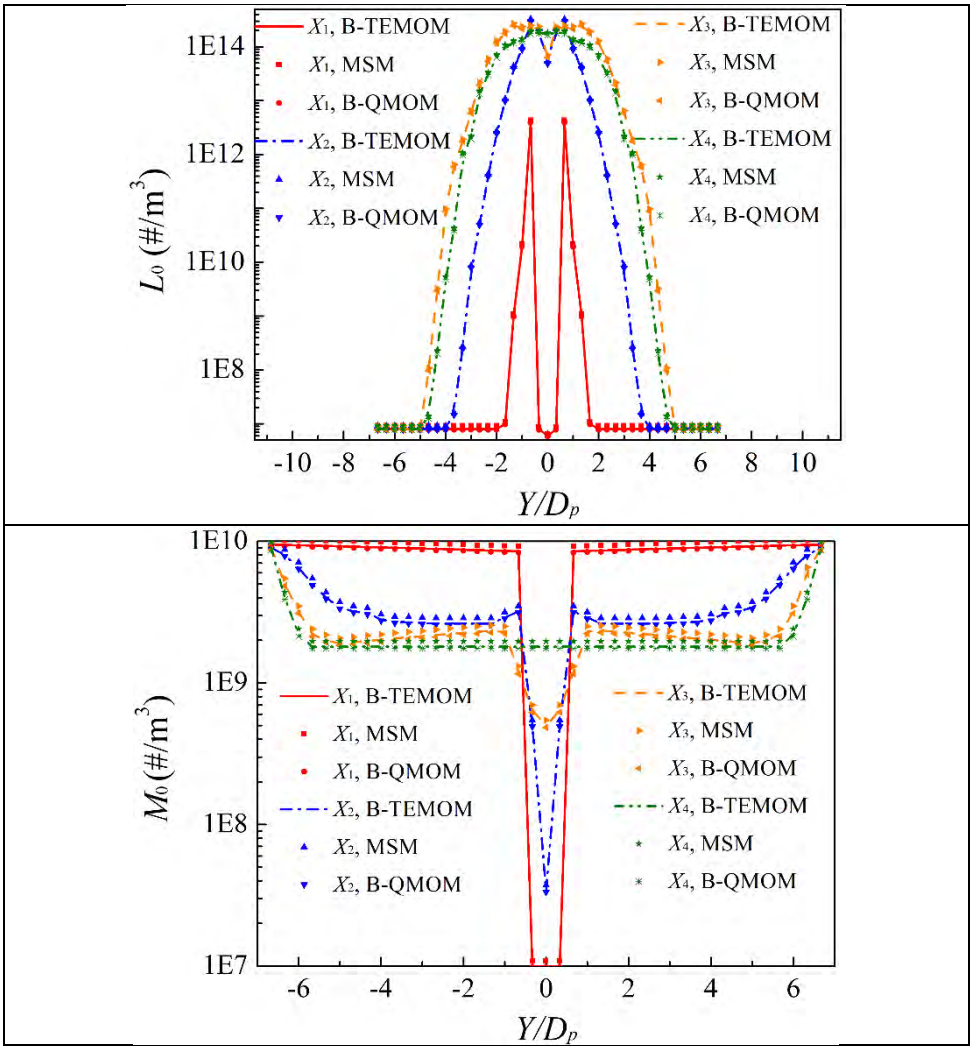

Fig. 3. Comparison of the concentration distributions of background (M_o) and vehicle exhaust (L_o) particles simulated with the bimodal Taylor expansion method of moments (B-TEMOM), moving sectional method (MSM) (Tsantilis et al., 2002), and the bimodal quadrature method of moments (B-QMOM) (McGraw, 1997) in the *YZ* plane with $Z = 0$ m and $X \leq 1$ m (i.e., $X_1 = 0.005$ m, $X_2 = 0.25$ m, $X_3 = 0.5$ m and $X_4 = 1$ m), where D_p is the diameter of the vehicle tailpipe.

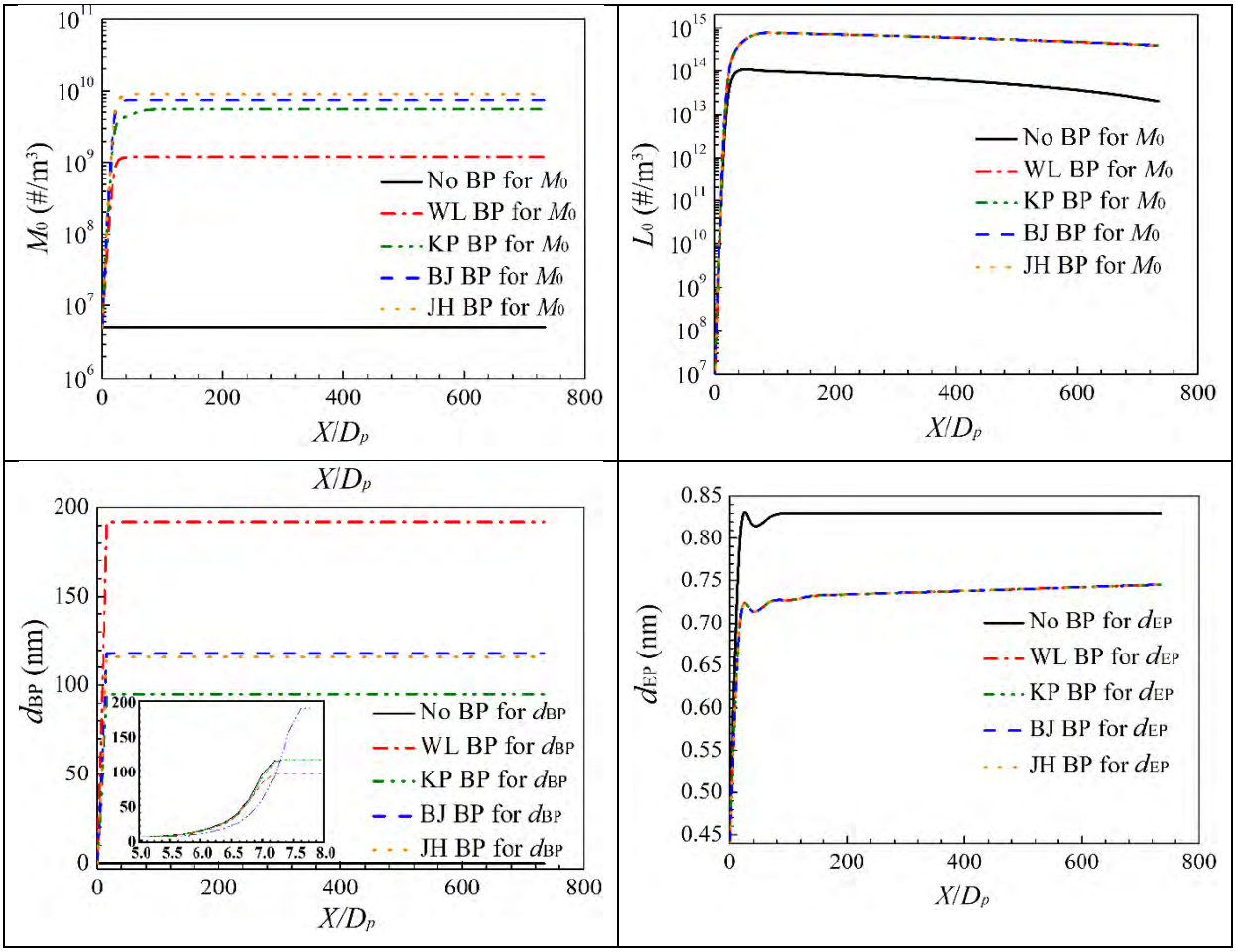

Fig. 4. Variations of concentrations and diameters of vehicle exhaust particles (L_o, d_{EP}) and background particles (M_o, d_{BP}) with non-dimensional axial distance from the tailpipe exit for different background particles (BP) representing various locations in China (WL, Wenling; KP, Kaiping; BJ, Beijing; JH, Jinhua; Table 2).

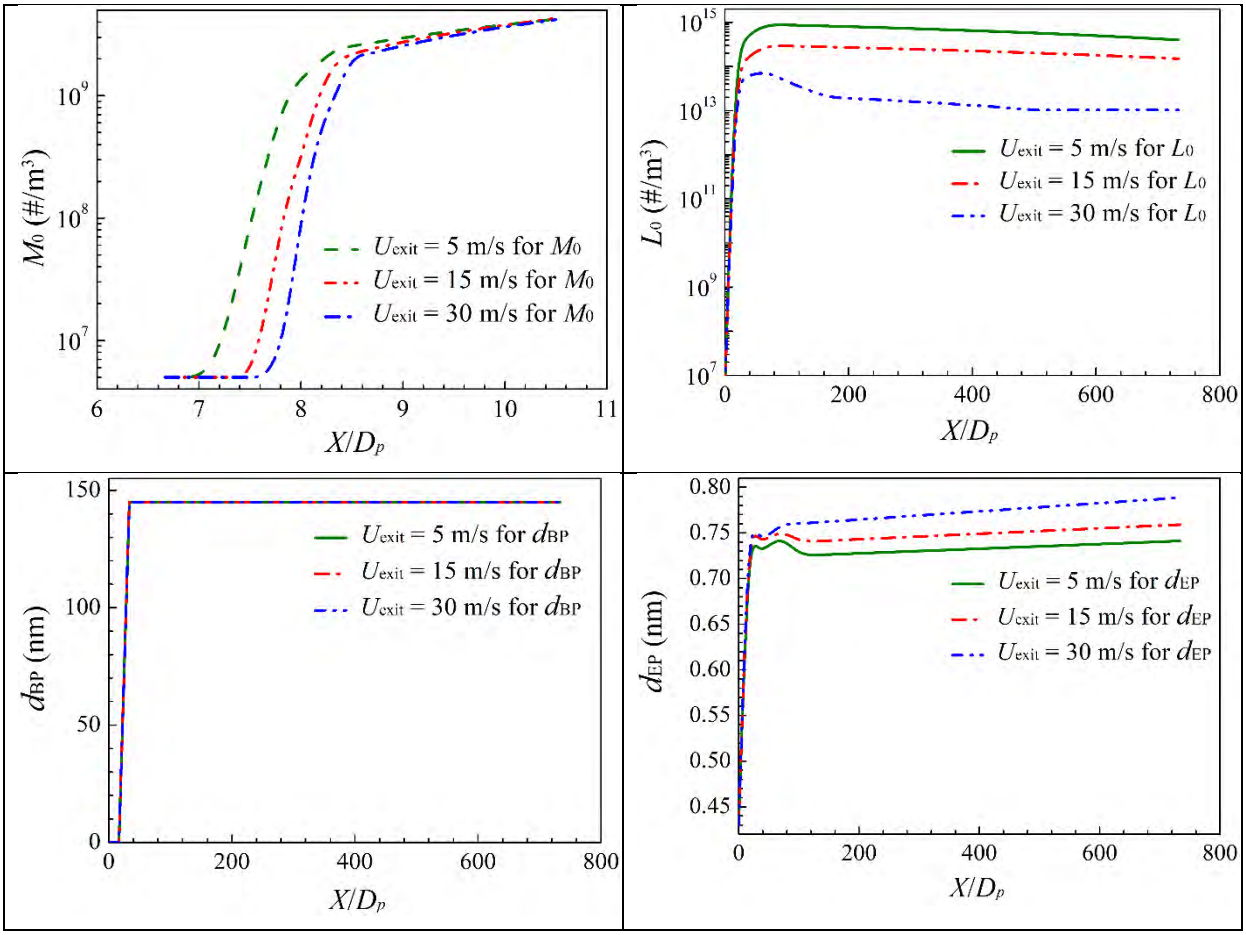

Fig. 5. Variations of concentrations and diameters of vehicle exhaust particles (L_o, d_{EP}) and background particles (M_o, d_{BP}) with non-dimensional axial distance from the tailpipe exit for different tailpipe exit velocities (U_{exit}) ranging from 5–30 m/s.

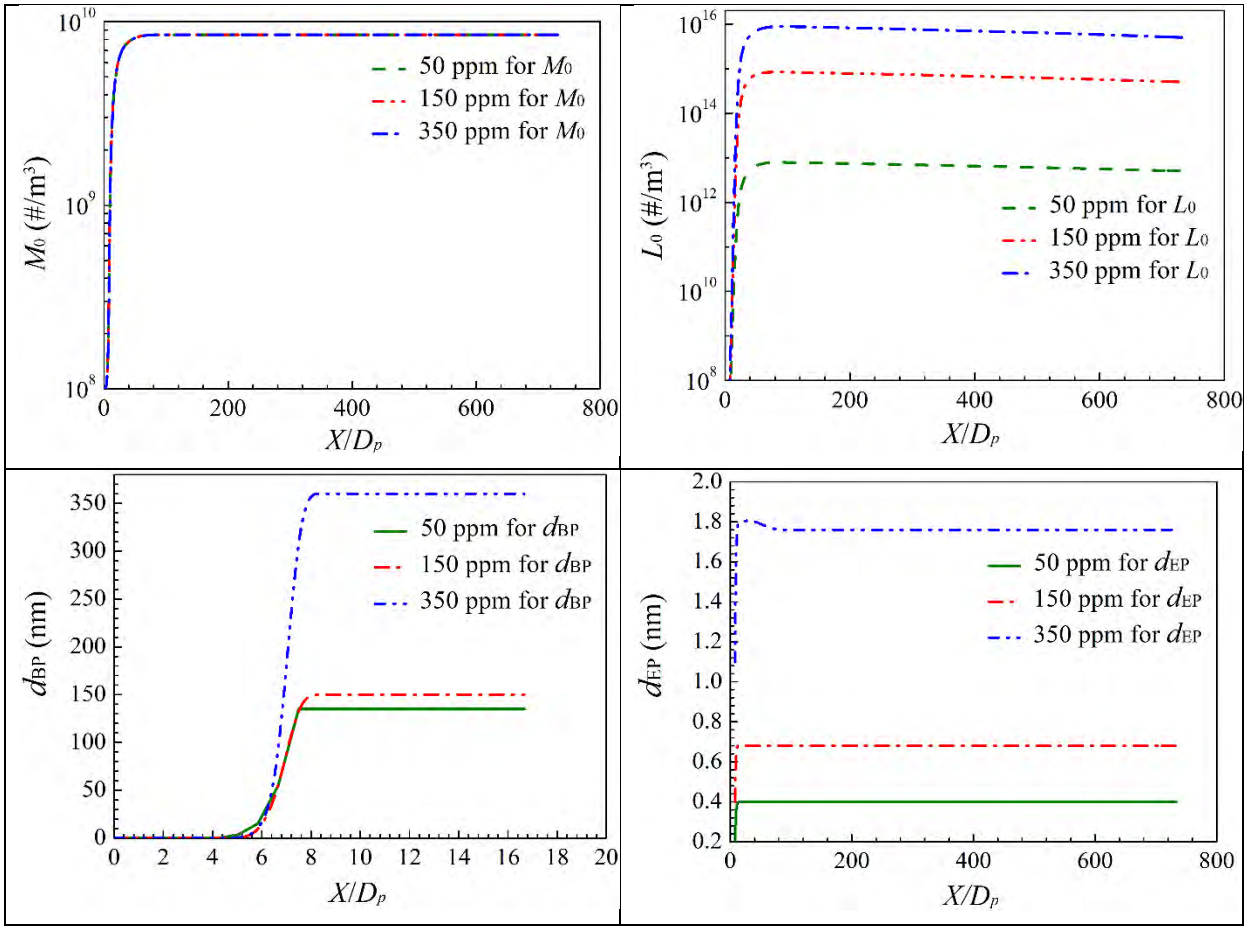

Fig. 6. Variations of concentrations and diameters of vehicle exhaust particles (L_o, d_{EP}) and background particles (M_o, d_{BP}) along the exhaust jet stream (i.e., axial direction X) for different sulfur contents ranging from 50–350 ppm.

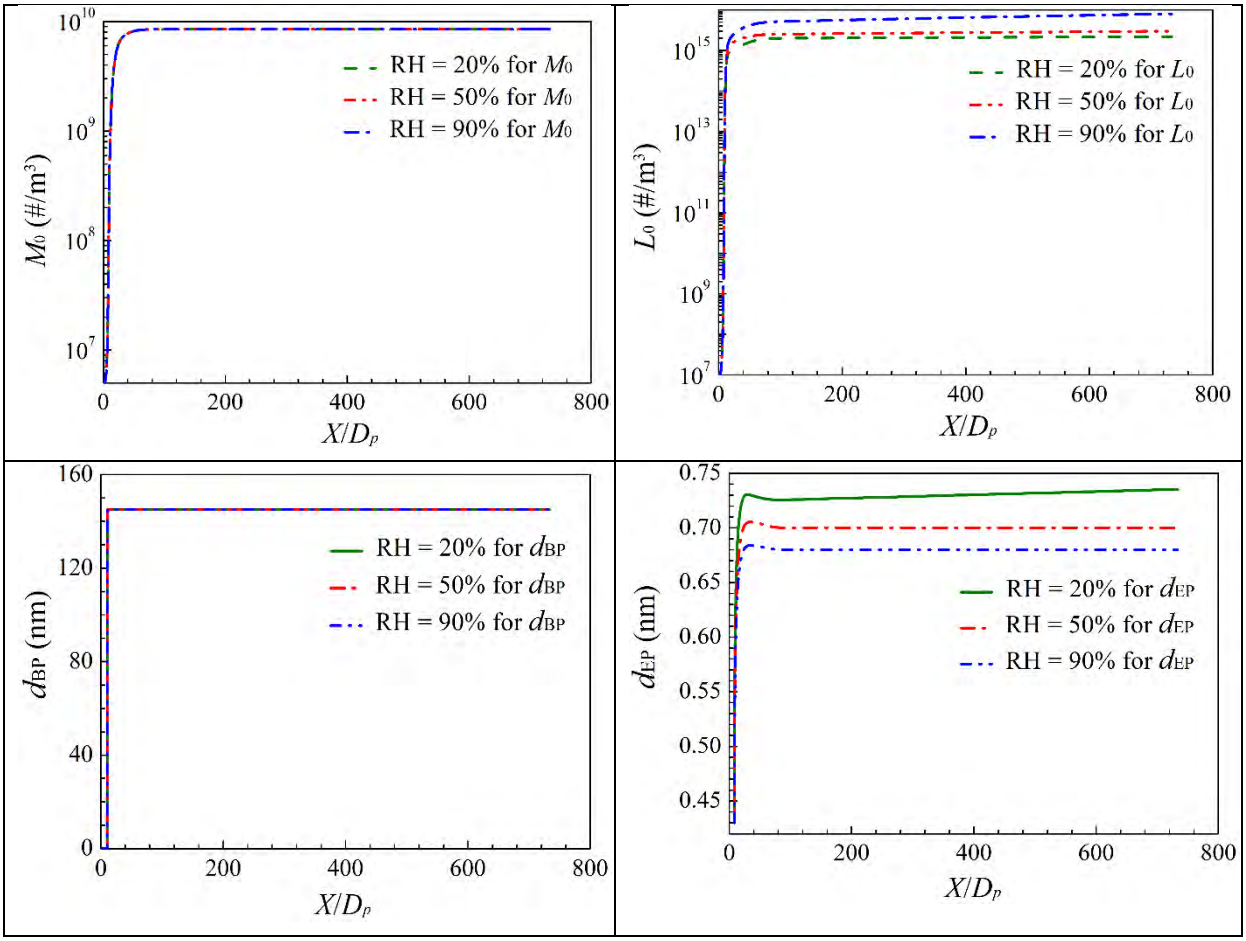

Fig. 7. Variations of concentration and diameter of vehicle exhaust particles (L_o, d_{EP}) and background particles (M_o, d_{BP}) along the exhaust jet stream (i.e., axial direction X) **for** different ambient relative humidities (RH) ranging from 20 to 90%.

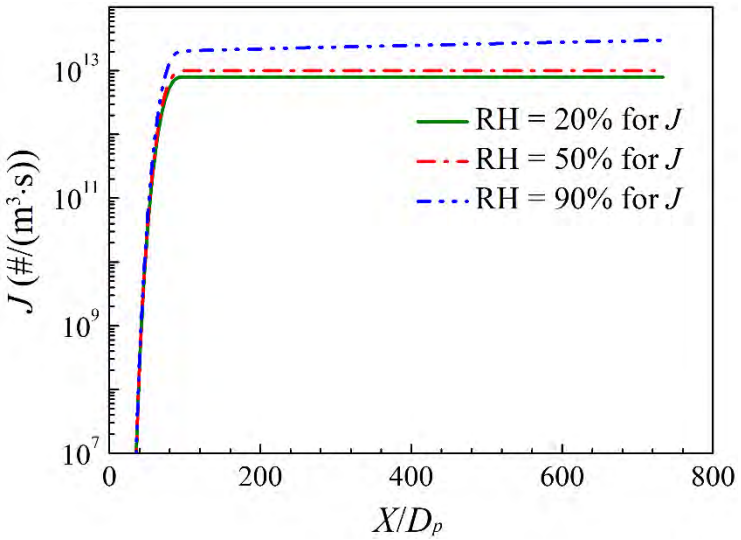

Fig. 8. Variations of particle nucleation rate (J) along the exhaust jet stream (i.e., axial direction X) for different ambient relative humidities (RH) ranging from 20 to 90%

Tables

Table 1 Main model parameters for the two-dimensional and three-dimensional numerical models

Type	D_p (mm)	L_p (mm)	D_f (m)	L_f (m)	N ($\times 10^4$)
3-D	60	70	0.4	2.0	53.63
2-D	60	70	20	60	8.60

D_p and L_p are the diameter and length of the vehicle tailpipe; D_f and L_f are the diameter and length of the far-field in the computation domain.

Table 2 Parameters of simulated background particles for different locations in China (Wu et al., 2008; Peng et al., 2014)

Type	Site	Mode	d_p (nm)	N (#/cm^3)	σ	M_0*($\times 10^{-7}$)	M_1*	M_2*($\times 10^{10}$)
Urban	Jinhua (JH)	Aitken mode	116	10,753	1.6	2.15	14.2	6.82
Urban	Beijing (BJ)	Accumulation mode	117	9,400	1.9	1.88	30	19.6
Regional	Kaiping (KP)	Aitken mode	95	6,883	1.81	1.38	21.31	7.84
Coastal	Wenling (WL)	Accumulation mode	192	1,413	1.63	0.28	21.68	14.3

NB: d_p is the geometric mean diameter of particles, N is the particle concentration, σ is the geometric standard deviation of particles, M_0*, M_1*, and M_2* are the first, second and third order dimensionless moments of particles.